



Seismic signatures of a hydrated mantle wedge from antigorite crystal-preferred orientation (CPO)



Sarah J. Brownlee^{a,*}, Bradley R. Hacker^{a,b}, George E. Harlow^c, Gareth Seward^a

^a Earth Research Institute, University of California, Santa Barbara, CA, USA

^b Department of Earth Science, University of California, Santa Barbara, CA, USA

^c Department of Earth and Planetary Sciences, American Museum of Natural History, New York, NY, USA

ARTICLE INFO

Article history:

Received 22 August 2012

Received in revised form

26 April 2013

Accepted 3 June 2013

Editor: L. Stixrude

Available online 28 June 2013

Keywords:

antigorite

seismic anisotropy

subduction

electron backscatter diffraction (EBSD)

CPO

LPO

ABSTRACT

We report electron backscatter diffraction (EBSD) measurements of antigorite crystal preferred orientations (CPOs) from 7 samples of antigorite schist from serpentinite mélanges adjacent to the Motagua fault system in central Guatemala. The CPOs range from diffuse girdle to point distributions of (001)_{atg}. Girdle distributions of (001)_{atg} are not expected from deformation theory or experiments, suggesting that they are a result of growth rather than deformation, and may thus be topotactically related to the CPO of the olivine from which the antigorite grew. The calculated seismic anisotropy ranges from 6% to 28% in V_p , and 5% to 33% in V_s , and is highest for samples with a point maximum of (001)_{atg}. For all samples the minimum V_p corresponds to the pole to (001)_{atg}, and the maximum V_p occurs within the foliation for samples with a clearly defined foliation. Trench-parallel shear-wave splitting observations for subduction zones can best be explained by a combination of olivine B-type CPO and antigorite oriented with (001) parallel to the foliation; only a relatively thin (~20 km) zone of hydrated mantle is required to explain the observed splitting times.

© 2013 Elsevier B.V. All rights reserved.

1. Introduction

Hydration/dehydration reactions in the mantle wedge and slab of subduction zones have important effects on seismicity and seismic velocity, including velocity anisotropy (e.g., Hacker et al., 2003; Kneller et al., 2007; Rabbel et al., 2011). For instance, antigorite schist along the base of the mantle wedge has been proposed to explain trench-parallel fast shear-wave polarization planes observed in subduction zones (e.g. Katayama et al., 2009). Olivine B-type CPO, which can form in water-saturated conditions (Jung and Karato, 2001), has been suggested to contribute to trench-parallel shear-wave splitting in the fore-arc portion of mantle wedge (Kneller et al., 2007). Dehydration reactions in the subducting slab have been proposed to explain the double seismic zone observed in many subduction zones (Hacker et al., 2003; Brudzinski et al., 2007). The distribution of hydrous minerals within a subduction zone can be studied directly using seismic imaging if the seismic properties of hydrous minerals are significantly different from those of anhydrous minerals. This study investigates the effects of hydration in the mantle wedge of

subduction zones by measuring the crystal-preferred orientation (CPO) of antigorite schists from the mélange adjacent to the Motagua fault system in central Guatemala.

2. Methods

2.1. Samples

Antigorite schist was collected from serpentinite mélanges adjacent to the Motagua fault system in central Guatemala (Fig. 1) as part of a study of the Guatemala Suture Zone (e.g., Harlow et al., 2006, 2011; <http://research.amnh.org/eps/jade>). Small chips (~3 × 3 × 1 cm³) were cut from samples that have “relatively coarse” antigorite prisms in thin section (Table 1), selected by GEH from the American Museum of Natural History (AMNH) collection. All but one sample (MVE03-60) come from the mélange north of the fault (Brueckner et al., 2009; Flores et al., 2010), however, except for subtle differences in assemblage statistics (Harlow et al., 2006, 2010), these antigorite schists from both sides of the fault are very similar. The samples are almost 100% antigorite with only a few vol% carbonates, oxides, and sulfides, talc and chlorite (Table 1); phases were identified with a combination of powder X-ray diffraction and microprobe analysis supported by optical petrography, plus the EBSD and EDS observations made in this study. Standard (30 μm thick) thin

* Corresponding author. Tel.: +1 313 577 6223.

E-mail addresses: sarah.brownlee@wayne.edu, brownlee.sj@gmail.com (S.J. Brownlee).

¹ Now at: Department of Geology, Wayne State University, Detroit, MI, USA.

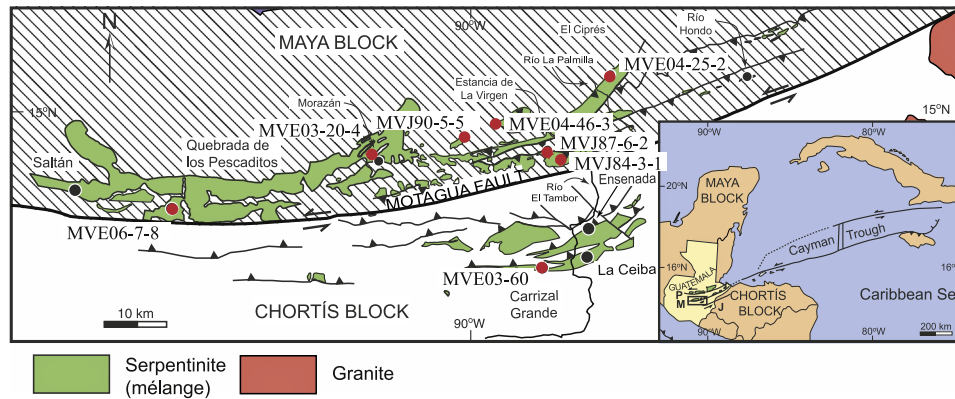


Fig. 1. Locations (red dots) of the studied antigorite samples from the Motagua fault zone of central Guatemala. (For interpretation of the references to color in this figure legend, the reader is referred to the web version of this article.)

Table 1
Sample locations and descriptions.

Sample ID	Lat/Lon	Description
MVE03-60	14.848 N/89.940 W	Fine-grained antigorite serpentinite with minor (< 1–3%) magnesite, talc, chromite, and Ni-sulfides. Dolomite (in vein; < 1% of total) identified by EDS and EBSD. Talc intergrown with antigorite caused polishing problems. Mixed brittle deformation with shear crystallization of atg; weak foliation, no lineation.
MVE04-25-2	15.012 N/89.816 W	Mixed medium- (~100 μm \times 5 μm) and fine-grained (< 50 μm \times 1 μm) antigorite serpentinite with minor Mg-chlorite, talc, chromite, Mn-ilmenite, Fe-Ni-sulfides, and dolomite. Mare's tail and cross vein Atg.
MVJ90-5-5	14.946 N/90.007 W	Little deformation, late brittle fracturing; weak foliation, no lineation. Fine-grained (~100 μm \times 2–5 μm needles) antigorite serpentinite with minor brucite, magnesite, Mn-ilmenite, pentlandite, and dolomite. Splaying bundles of antigorite, magnesite, and dolomite.
MVE04-46-3	14.991 N/89.958 W	Little deformation; weak foliation, no lineation. Fine-grained (~100 μm \times 2–5 μm) antigorite serpentinite with minor Mn-ilmenite. Mesh texture Atg.
MVJ87-6-2	14.941 N/89.885 W	Recrystallized (?); weak foliation, no lineation. Medium-grained (~200 μm \times 20 μm) antigorite serpentinite with minor magnetite, Mn-ilmenite, and dolomite. Mesh texture Atg.
MVE06-7-8	14.853 N/90.343 W	Recrystallized (?); weak foliation, no lineation. Medium (~150 μm \times 50 μm) to fine-grained (< 10 μm) antigorite serpentinite with minor magnesite, magnetite, pentlandite, pyrrhotite, and Ni metal.
MVJ84-3-1	14.942 N/89.852 W	Brittle deformation (?) w/recrystallized Atg (?); weak foliation, no lineation. Medium (~200 μm \times 50 μm) to fine-grained (~100 μm \times 5 μm) antigorite schist with minor magnesite and chromite.
MVE03-20-4	14.940 N/90.164 W	Identifiable foliation, weak lineation defined by preferred orientation of antigorite grains in thin section. Medium-fine-grained (100 μm \times 50 μm) antigorite serpentinite with minor magnesite, talc, chromite, Mn-ilmenite, pyrite, and dolomite.
		Recrystallized mylonite; strong foliation, weak lineation defined by elongated antigorite needles in thin section.

sections were prepared for each sample. We attempted to cut each thin section parallel to the foliation and lineation, but the foliation was difficult to discern in most samples due to fine grain size. The thin sections were polished to 0.25 μm smoothness using diamond polish, and further polished to ~10 nm smoothness using colloidal silica for ~1–2 h. Because antigorite is very soft, all polishing was done incrementally by hand, on a sample-by-sample basis.

2.2. Electron backscatter diffraction (EBSD)

EBSD measurements were made at UCSB in an FEI Quanta 400F scanning electron microscope with a field-emission gun and an Oxford Instruments EBSD camera, using HKL Channel 5 software. The samples were not coated with carbon. EBSD patterns were collected in low vacuum (50–70 Pa), using an accelerating voltage of 20 kV, a spot size of ~1 μm , working distances of 10–15 mm, and with the sample tilted 20° to the incident beam. EDS data were collected simultaneously during EBSD mapping, and were used to ensure proper indexing of patterns. A match unit for EBSD indexing of antigorite was created from the structural data in Capitani and Mellini (2004). A maximum of 7 bands were detected and between 50 and 70 reflectors were used for indexing. The Channel 5 software uses a Hough transform for automated band detection (e.g., Krieger Lassen, 1998; Day, 2008), and Hough

space resolution was set between 95 and 110. Three background frames were measured, and 2-by-2 binning was used in the images.

Two types of EBSD maps were made for each thin section. A fine-scale (1–2 μm step size) map was made to image the microstructure at high resolution. The fine-scale maps also allowed assessment of the quality of the polishing and EBSD indexing rates. The fine-scale band-contrast map gave a good measure of the quality of the EBSD patterns being recorded, and provided an excellent image of the microstructure even when indexing rates were low. No post-processing 'cleaning' has been applied to any of the fine-scale EBSD maps, and indexing rates reported are for raw data. In addition to the fine-scale EBSD map, a coarse map (~100 μm step size) was measured for the purpose of getting 1-point-per-grain measurements across as much of the thin section as possible for determination of crystal preferred orientation (CPO). A coarse map was not measured for MVE03-60 because little of the sample produced detectable EBSD patterns.

2.3. Seismic-velocity calculations

Seismic velocities were calculated using the method described in Mainprice (1990) as implemented in the FORTRAN software written by David Mainprice. All velocity calculations were done using the CPOs determined from the coarse EBSD maps because

the samples are heterogeneous at a smaller scale. All the samples have more than 95 vol% antigorite; other phases have little effect on the seismic properties of the rock, and were therefore not included in the calculations. The stiffnesses, C_{ij} , for antigorite are from Bezacier et al. (2010). Voigt–Reuss–Hill (VRH) averaging was used.

3. Results

3.1. Fine-scale structure

Fine-scale band contrast and Euler angle maps are shown in Fig. 2. Indexing rates were roughly inversely proportional to grain size in all samples. The samples with the finest grain size, such as MVE04-25-2 and MVE04-46-3, had the lowest indexing rates because the fine grains have proportionally more grain boundaries, which are more strongly etched by the colloidal silica polish.

3.1.1. MVE03-20-4—81% indexed

This sample was cut parallel to the foliation, and had the highest indexing rate for a fine-scale map. The antigorite crystals are fairly uniform in size and bladed rather than acicular (Fig. 2A). The lath long axes define the lineation. Twins parallel to the long axes of the crystals are evident in the band-contrast image. Some mis-indexing is apparent because the basal plane of antigorite is nearly trigonal and

the subtle differences in the diffraction patterns are not sufficiently distinct for the automated indexing routine.

3.1.2. MVE06-7-8—64% indexed

This sample has a bimodal grain-size distribution (Fig. 2B). The very fine-grained ($< \sim 5 \mu\text{m}$) portions are not well polished, whereas the larger grains ($100\text{--}200 \mu\text{m}$) are very well polished, and may represent vein growth of antigorite after transformation of the protolith to antigorite. The indexing rate on the larger grain sizes is $> 95\%$, whereas it is $\sim 25\%$ for the smaller grains. The large grains are lath-shaped, whereas the finer grains are acicular. Twins are evident in many of the larger grains. This thin section is subparallel to the foliation; there is no evident lineation, which suggests static growth in a hydrodynamic vein environment.

3.1.3. MVJ87-6-2—45% indexed

The grains in this sample range from equant to acicular (Fig. 2C). A grain of magnesite in the upper left corner of this map was confirmed by EDS and EBSD. The acicular grains do not have a distinct shape preferred orientation. This thin section is subparallel to the foliation; there is no evident lineation.

3.1.4. MVJ84-3-1—34% indexed

This sample was cut subparallel to the foliation. The grains are quite large ($100\text{--}200 \mu\text{m}$) (Fig. 2D). The large grains did not polish

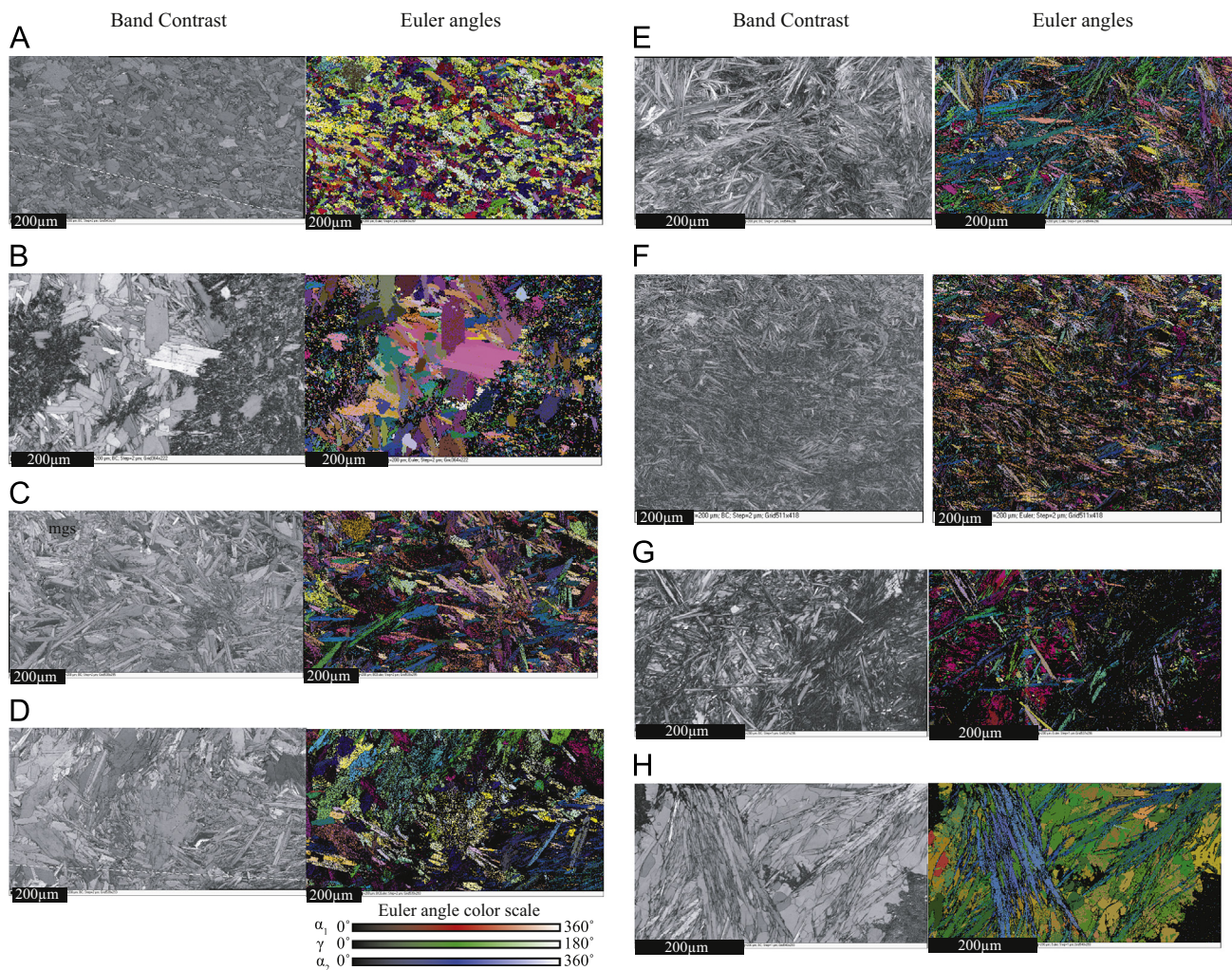


Fig. 2. Band contrast and Euler angle images of the fine-scale EBSD maps show a range of microstructure. (A–D) Bladed antigorite. (E–G) Acicular antigorite. (H) Dolomite +antigorite vein. Dashed lines indicate identified lineation. (A) MVE3-20-04, (B) MVE06-7-8, (C) MVJ87-6-2, (D) MVE84-3-1, (E) MVJ90-5-5, (F) MVE04-46-3, (G) MVE04-25-2 and (H) MVE03-60.

well, and certain orientations indexed better than others (e.g., the twinned grain in the bottom left corner). The finer grains form a weak lineation.

3.1.5. MVJ90-5-5—49% indexed

This sample consists of antigorite needles splayed in a feathery or interpenetrating pattern (Fig. 2E). There may be a slight preferred alignment of the long axes of the needles (detected by eye) from the bottom left to the upper right of the map. This sample did not display a well-defined foliation, so the thin section orientation is uncertain. The very fine-grained portions of this thin section also did not polish or index well, but the larger crystals are well indexed.

3.1.6. MVE04-46-3—35% indexed

This sample has a texture similar to that of MVJ90-5-5, with radiating sprays of crystals (Fig. 2F). It is slightly finer grained than MVJ90-5-5, and the map was made at a lower resolution (2 μm instead of 1 μm steps). These factors combined to weaken the band contrast image, and reduced the indexing rate; however, the textural similarities between the two samples are clear.

3.1.7. MVE04-25-2—23% indexed

This sample has a unique texture (Fig. 2G). Misorientation angles of $\sim 60^\circ$ and $\sim 90^\circ$ between adjacent grains are abundant, and may reflect an inherited topotaxy or epitaxy. Fine grains are not well indexed.

3.1.8. MVE03-60—70% indexed

Even after extensive polishing, only a dolomite+antigorite vein in this sample produced detectable EBSD patterns. The EBSD data from this fine-scale map (1 μm step size) reveal intergrown antigorite and dolomite; both have a strong preferred orientation (Fig. 2H).

3.2. Crystal preferred orientations (CPOs) from coarse EBSD maps

There are two types of antigorite CPOs (Fig. 3). The first type has a weak (001) maximum within a diffuse girdle. The two samples that best typify this type of CPO, MVJ90-5-5 and MVE04-25-2 are massive aggregates of acicular crystals. The other type of CPO has a strong (001) maximum perpendicular to the foliation, and is exemplified by the two samples that have strong foliations (MVE03-20-4 and MVJ84-3-1). The other 3 samples have CPOs intermediate between these two types. For all but one sample, MVE84-3-1, the [010] maximum is stronger than the [100] maximum. In MVE03-20-4, [010] is parallel to the lineation; however, in MVJ84-3-1, [100] is parallel to the weakly defined lineation. A lineation was not identifiable in any of the other samples.

Dolomite in sample MVE03-60 has a (0001) maximum, and a girdle of (a) directions (Fig. 4), typical of dolomite (Higgs and Handin, 1959; Delle Piane et al., 2009). The antigorite (001) planes define two maxima, subparallel to dolomite (0001).

3.3. Velocity calculations

Single crystals of antigorite have high velocity anisotropy (Bezacier et al., 2010), similar to other sheet silicates such as lizardite (Auzende et al., 2006), biotite (Aleksandrov and Ryzhova, 1961), and muscovite (Vaughan and Guggenheim, 1986). Although the crystal structure of antigorite is monoclinic, its velocity anisotropy is nearly uniaxial (Bezacier et al., 2010). The velocity calculations for all samples except MVE03-60 (dolomite vein) are shown next to their respective CPOs in Fig. 3. As expected, the

samples with weaker CPOs tend to have the slowest maximum P-wave velocities and the least anisotropy in V_P and V_S . The V_P symmetry in the samples with the weakest CPOs is orthorhombic, but uniaxial in the samples with stronger CPOs. The slow V_P direction corresponds to the (001)_{atg} maximum and the fast V_P direction to [010]_{atg}. The V_S symmetry is similar, but more irregular and of smaller magnitude.

4. Discussion

4.1. Origin of antigorite CPOs

Antigorite CPOs can arise from a range of processes, including those related to deformation, such as dislocation glide and grain rotation, and those related to crystal growth, such as topotaxy or growth by void-filling. The different CPO-forming processes produce markedly different CPOs (Fig. 5). The following discusses measured CPOs in the context of CPOs expected from deformation, and growth-related processes.

Antigorite is a sheet silicate with a monoclinic crystal structure ($a=43 \text{ \AA}$, $b=9.3 \text{ \AA}$, $c=7.3 \text{ \AA}$, $\beta=91^\circ$; Capitani and Mellini, 2004). The sheets are in the (001) orientation, such that dislocation glide and grain rotation are both expected to rotate (001) parallel to the shear plane, and, indeed, this has been observed in experimentally and naturally deformed samples (e.g., Katayama et al., 2009; Bezacier et al., 2010; Hirauchi et al., 2010; Van de Moortele et al., 2010; Padrón Navarta et al., 2012). The two Motagua samples with a clear foliation also show (001) parallel to the foliation. Within the (001) plane, the [010] direction has the shortest unit cell dimension, is known to accommodate $b/3$ stacking faults (Aruja, 1945) and might thus be expected to be the dominant slip direction. Hirauchi et al. (2010), indeed, found that [010] preferentially oriented parallel to the lineation in two of the three serpentinite samples they measured from the Izu–Bonin forearc; those samples have maxima with strengths of 5–7 multiples of uniform distribution (m.u.d.).

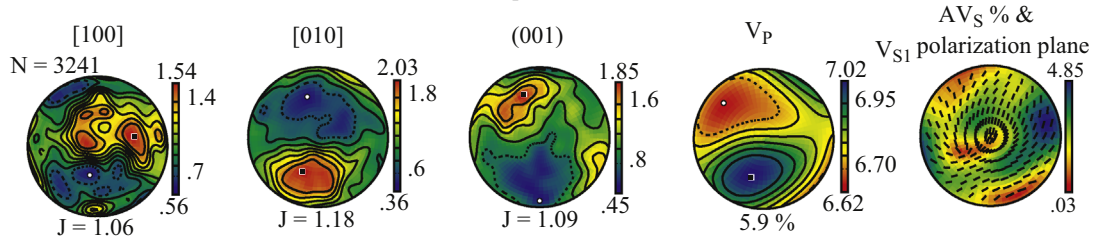
The antigorite structure has asymmetric, 43 \AA -wavelength corrugations with axes of curvature parallel to [010]. With additional bond rearrangement, slip in the [100] direction, with a Burgers vector of $a/17$ might be possible. Katayama et al. (2009), for example, observed alignment of [100] subparallel to the shear direction in two experimentally deformed antigorite samples (m.u.d.s of 4–5). Bezacier et al. (2010) found [100] and [010] maxima subparallel to the lineation in one Cuban serpentinite (again, with ~ 7 m.u.d.), suggesting that two slip systems/deformation mechanisms were active.

The two Motagua samples with a clearly defined foliation and lineation each have a point maximum of (001) parallel to the foliation. MVE03-20-4 has a diffuse [010] maximum parallel to the lineation, similar to that reported by Hirauchi et al. (2010), implying [010](001) slip. The second, MVJ84-3-1, has a [010] maximum parallel to the lineation, but also a [100] maximum parallel to the lineation, similar to that reported by Bezacier et al. (2010), implying mixed [100](001) and [010](001) slip. The rest of the Motagua samples have similarly strong [100] and [010] maxima, compatible with any of the aforementioned slip systems; however, their (001) distributions vary, suggesting that additional processes were active.

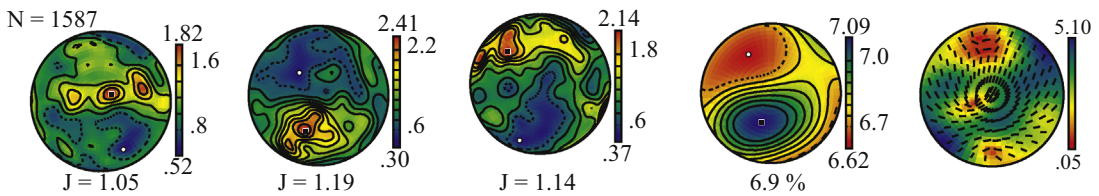
Boudier et al. (2010) noted that antigorite CPOs need not necessarily be the result of deformation, but might instead result from topotactic growth of antigorite on olivine and thereby inherit the orientation of the host. They measured crystallographic relationships between olivine and antigorite, finding that (010)_{atg} is always parallel to (001)_{ol}, and that (001)_{atg} is dominantly parallel to (100)_{ol}—or secondarily parallel to (010)_{ol}. These two

A

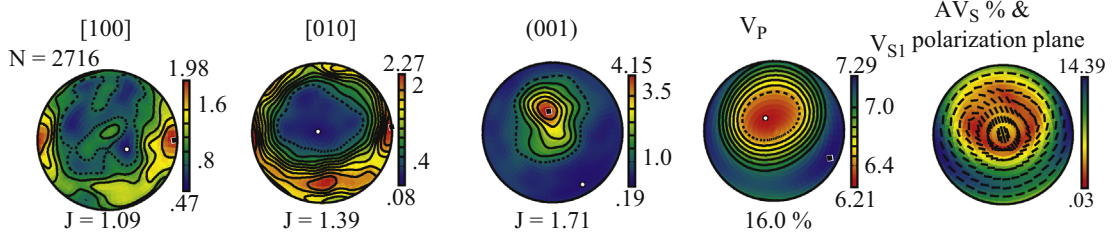
foliation not obvious in these chips, lineation could not be determined.



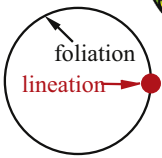
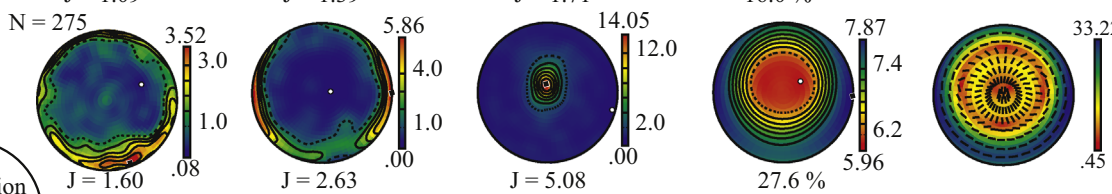
B



C

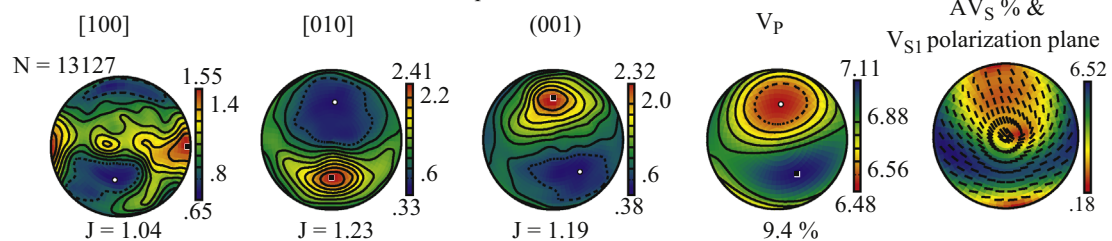


D

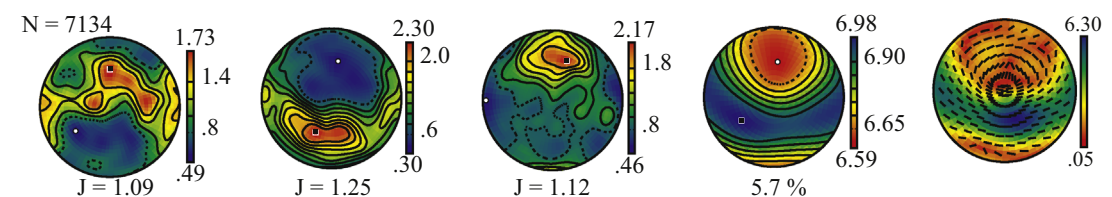


foliation not obvious in these chips, lineation could not be determined.

E



F



G

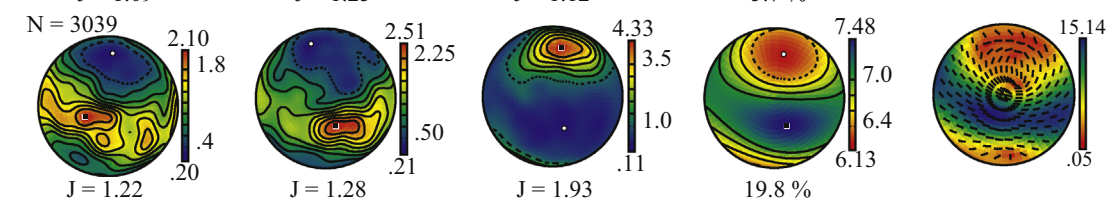


Fig. 3. Coarse EBSD maps have two types of CPO that range in strength from 2% to 14% m.u.d. (multiples of uniform distribution); calculated velocities show a corresponding range in anisotropy from 5% to 15% (C_{ij} are listed in Supplementary Table 1). The reference frame of pole figures is foliation E–W on page, and lineation E, or for samples with weakly defined foliation and lineation long edge of thin section is oriented E–W on page. (A) and (B) CPOs with diffuse $(001)_{atg}$ girdles. (C) and (D) CPOs from samples with a clearly defined foliation have point distributions of $(001)_{atg}$ parallel to foliation. (E–G) CPOs that are a mixture of diffuse girdle and point distributions. (A) MVJ90-5-5, (B) MVE04-25-2, (C) MVE84-3-1, (D) MVE3-20-04, (E) MVE06-7-8, (F) MVJ87-6-2, and (G) MVE04-46-3.

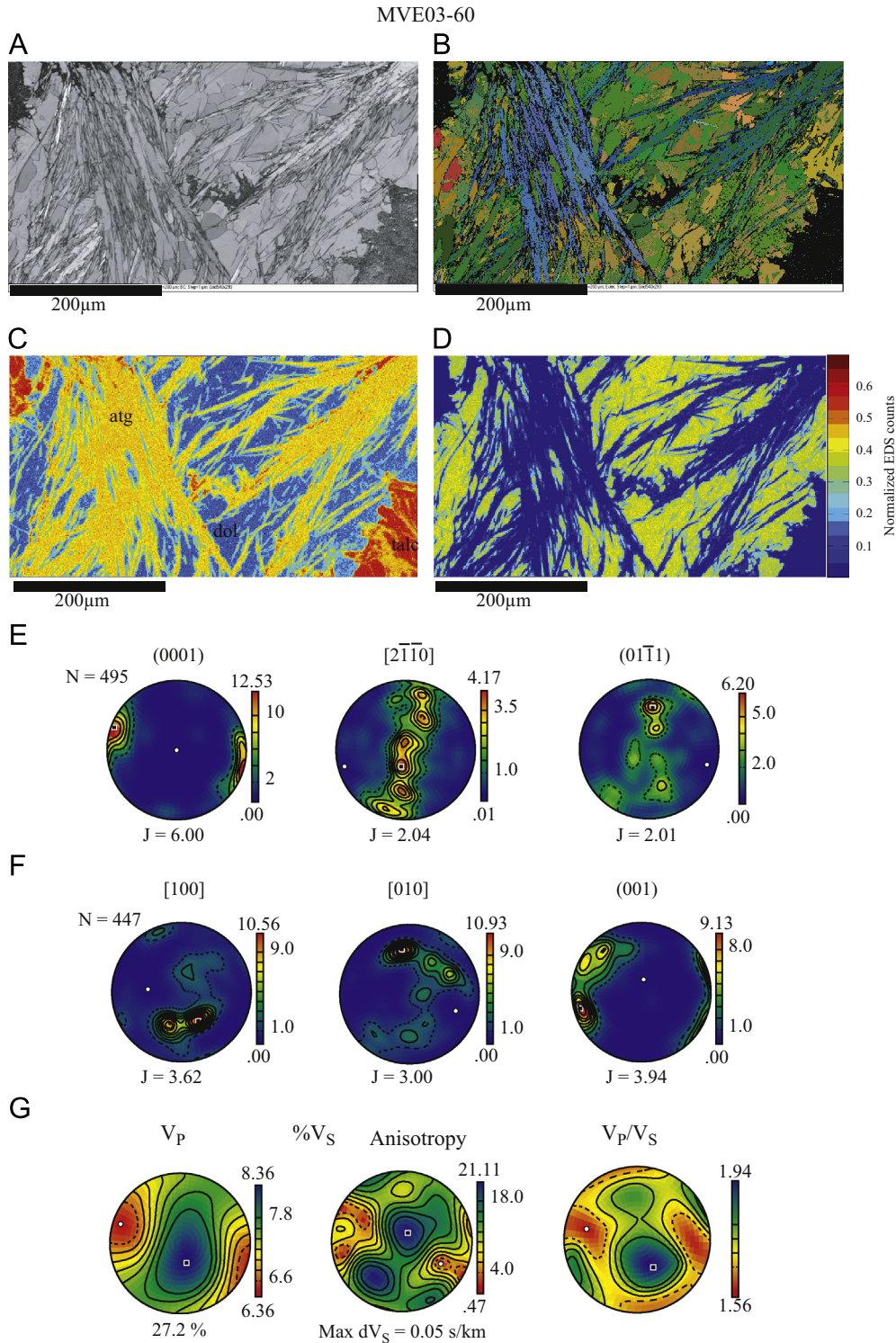


Fig. 4. Sample MVE03-60, a vein of intergrown antigorite+dolomite, has strong CPOs and strong anisotropy (C_{ij} are listed in Supplementary Table 1). (A) Band contrast image. (B) Euler angle image. (C), and (D) Normalized EDS counts for Si, and Ca. (E) and (F) Lower hemisphere pole figures of dolomite and antigorite CPOs. (G) Lower hemisphere plots of V_p , % V_S anisotropy, and V_p/V_S for the aggregate.

topotactic orientations of antigorite in olivine suggest that a bimodal or girdle distribution of $(001)_{atg}$ might develop in antigorite overgrown in olivine with a strong CPO. $(001)_{atg}$ girdles have been observed previously (Soda and Takagi, 2010; Nishii et al., 2011), and are not expected to form due to dislocation creep, for the reasons outlined above. Both of the Motagua samples that display a girdle of $(001)_{atg}$ also have a fairly strong $[010]_{atg}$ maximum, which might have developed from the $[001]_{ol}$ of the pre-

cursor olivine. Alternatively, antigorite can grow on lizardite or chrysotile (Evans, 1977). Livi and Veblen (1987) noted antigorite offsets, or modulations forming in lizardite at 60° angles to one another, similar to what we observe at a larger scale in sample MVE04-25-2.

In addition to overgrowth and replacement, antigorite serpentinites may form as veins from fluid infiltration into brittle fractures in the mantle wedge, analogous to the formation of

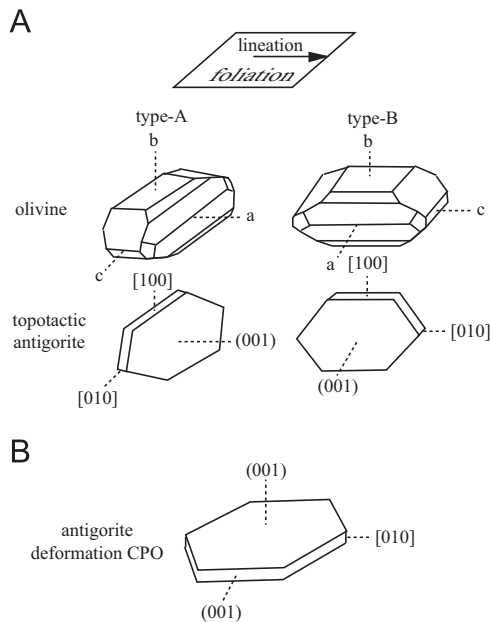


Fig. 5. A schematic illustration of expected olivine and antigorite orientations for (A) topotaxy on olivine type-A and type-B CPO, and (B) antigorite deformation-induced CPO.

jadeitites in the study area (Harlow et al., 2011). This formation mechanism might produce a preferred orientation of antigorite as crystals nucleate and grow from the vein walls. This growth mechanism favors 90° angles between $(001)_{\text{atg}}$ planes and the vein walls (Groppo and Compagnoni, 2007), and would produce a girdle distribution of $(001)_{\text{atg}}$ parallel to the vein.

Regardless of the initial antigorite CPO, upon deformation, $(001)_{\text{atg}}$ girdles are expected to move toward a maximum orthogonal to the shear plane as observed in all experimentally deformed antigorite. The range of observed CPOs—from girdle to point distributions of $(001)_{\text{atg}}$ —in the Motagua samples is likely related to variable deformation of crystals that originally grew in a vein or topotactically on olivine.

4.2. Consequences for seismic imaging of subduction zones

Observations of shear-wave splitting are often interpreted in terms of the preferred orientation of olivine resulting from flow in the upper mantle; e.g. fast shear-wave polarization directions are often interpreted as indicating the flow direction (e.g., Wolfe and Silver, 1998; Jung and Karato, 2001; Conrad et al., 2007; Karato et al., 2008; Long, 2010)—in spite of the ambiguities inherent in using a 2D observation to draw inferences from an orthorhombic mineral. For subduction zones this interpretation can be complicated due to varying olivine CPOs in water-saturated conditions (e.g., Jung and Karato, 2001; Mehl et al., 2003), and/or the possibility of 3-dimensional mantle flow (e.g., Funicello et al., 2006). Trench-parallel shear-wave splitting delays of > 1 s have been observed in a number of subduction zones (e.g., Savage, 1999; Park and Levin, 2002; Nakajima and Hasegawa, 2004; Long and van der Hilst, 2006; Baccheschi et al., 2011). Kneller et al. (2008) modeled the seismic anisotropy due to olivine B-type fabric in the mantle wedge of the Ryukyu subduction zone and suggested that the presence of foliated antigorite may explain discrepancies between predicted and observed shear-wave anisotropy. Whether serpentinite can be called upon to explain anisotropy observed in the mantle wedges and slabs of subduction zones depends on whether the anisotropy of serpentinite reinforces or negates the anisotropy of peridotite. There are at least

five olivine CPO types that have been identified (e.g., Ben Ismail and Mainprice, 1998; Jung et al., 2006), although only four are orthorhombic, ‘plane-strain type’ (specifically, the type-D CPO is produced by $[100][0kl]$ slip equivalent to mixed type-A and type-E CPOs). Type-A fabrics are the most commonly observed in natural samples. Type-B may occur in mantle wedges as a result of elevated H_2O fugacity (Jung and Karato, 2001; Frese et al., 2003; Mizukami et al., 2004; Katayama et al., 2005; Skemer et al., 2006; Kneller et al., 2007; Katayama and Karato, 2008). Type-E CPOs have been described from the mantle section beneath the Talt-eetna arc in Alaska (Mehl et al., 2003). Before entering a subduction zone, oceanic upper mantle shows SKS splitting times of ~ 1 s with fast S-wave polarization directions roughly parallel to the absolute plate motion, except for some locations where the lithospheric mantle preserves a fossil fabric related to ridge spreading (Wolfe and Silver, 1998; Smith et al., 2001; Fontaine et al., 2005; Conrad et al., 2007). These SKS splits are compatible with type-A, C, and E olivine CPOs, in which the fast shear-wave polarization direction for vertically propagating waves corresponds to the horizontal mantle flow direction (Jung and Karato, 2001; Karato et al., 2008; Long, 2010). In many arcs the mantle wedge shows trench-parallel fast S-wave polarization directions, an observation that is compatible with type-B olivine CPO if 2D corner flow is assumed (Kneller et al., 2007, 2008; Karato et al., 2008). If, however, trench-parallel flow is invoked, the observed shear-wave splitting is compatible with type-A, C, and E olivine CPOs (e.g. Karato et al., 2008). The subsequent effects of hydration and growth of antigorite in the mantle wedge will depend on whether the antigorite CPO is due mainly to growth (i.e. topotaxy or crystallization from vein), or deformation.

4.3. Topotaxy

Because the dominant orientation of antigorite grown topotactically in olivine is $(001)_{\text{atg}} \parallel (100)_{\text{ol}}$ (Boudier et al., 2010), the fast direction of olivine is replaced by the slow direction of antigorite. The initial effect of this hydration is thus to negate the anisotropy produced by the olivine CPO. For a single crystal of olivine, replacement by antigorite in the dominant topotactic orientation ($(001)_{\text{atg}} \parallel (100)_{\text{ol}}$) results in drastic changes to the orientation and symmetry of the seismic velocity (Fig. 6A). The fast $[100]_{\text{ol}}$ direction becomes the slow $(001)_{\text{atg}}$ direction, and the velocity symmetry changes from orthorhombic to near uniaxial-slow. For olivine with a type-A CPO and a horizontal foliation, the V_S anisotropy for vertically propagating waves ($(V_{S1}-V_{S2})/\text{median}(V_{S1})$) decreases until ~ 25 vol% topotactic antigorite has grown, after which the V_S anisotropy rises to a maximum of $\sim 60\%$ (Fig. 6B). After ~ 40 vol% antigorite has grown, the S-wave anisotropy is higher for the olivine+topotactic antigorite than for the dry olivine single crystal. The V_{S1} polarization plane rotates 90° for waves propagating vertically (parallel to $[010]_{\text{ol}}$). In a real subduction zone setting, the effects of topotactic growth of antigorite will depend on a number of factors including: (1) the type and strength of the olivine CPO, (2) the flow field (or orientation of the foliation and lineation), (3) the shear-wave propagation direction, and (4) the relative dominance of topotactic growth over other types of antigorite growth.

4.4. Antigorite growth as veins

Antigorite forms 90° boundaries with less-anisotropic crystals, such as olivine (Evans, 1977), suggesting that antigorite growing in a vein is likely to form with (001) perpendicular to the vein wall. This is consistent with filamentous antigorite veins, in which the long axes of antigorite (most likely $[010]$) are perpendicular to the vein walls (Groppo and Compagnoni, 2007). This relationship

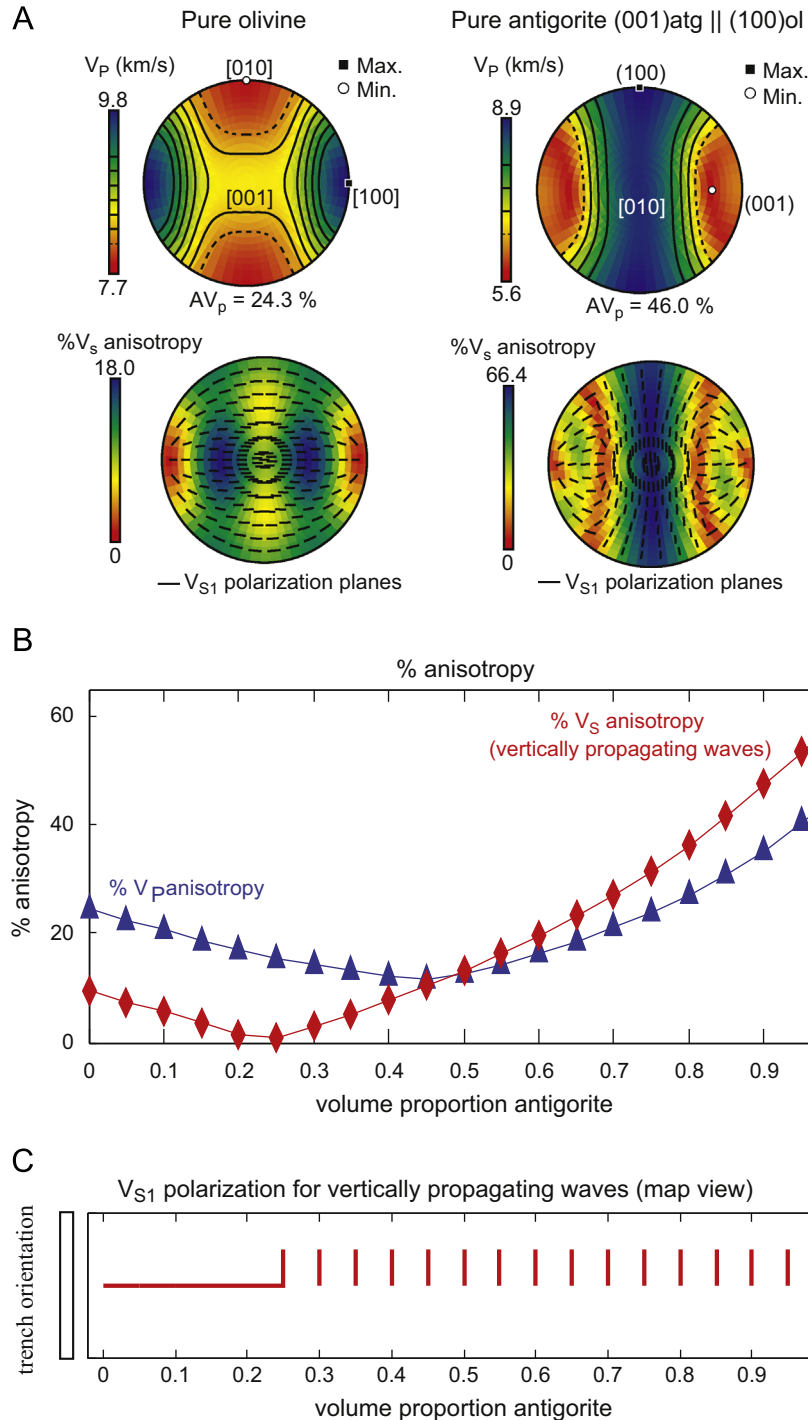


Fig. 6. The topotactic replacement of olivine by antigorite initially decreases velocity anisotropy, but total replacement leads to a 90° rotation of the S-wave polarization planes and a marked increase in anisotropy (C_j listed in Supplementary Table 1). (A) Lower hemisphere, equal area stereonets of V_P illuminate stark differences in symmetry and V_S anisotropy between olivine and antigorite. V_{S1} polarization planes rotate by ~90° for most propagation directions. (B) V_S anisotropy for vertically propagating waves (assuming horizontal foliation and olivine A-type CPO) decreases until ~25% of the olivine has been replaced by antigorite, then increases to maximum of ~60%. % V_P anisotropy decreases until ~40 vol% antigorite, then increases to maximum of ~46%. (C) V_{S1} polarization planes (shown in map view) for vertically propagating shear waves rotate by 90° at 25 vol% antigorite.

leads to a girdle distribution of (001). Because the direction perpendicular to (001) is the unique slow velocity direction in antigorite, a girdle distribution of (001) has the effect of drastically decreasing the anisotropy from the single-crystal or (001) point distribution CPO. This effect is observed in the velocity calculations for samples MVJ90-5-5 and MVE04-25-2, which display girdle-like distributions of (001). A true (001) girdle distribution would further decrease the velocity anisotropy.

4.5. Deformation-induced CPO

Theory and experiment both predict that deformation should align (001)_{atg} with the shear plane, and this has indeed been observed in naturally and experimentally deformed samples (e.g., Katayama et al., 2009; Hirauchi et al., 2010; Bezacier et al., 2010; Van de Moortele et al., 2010; this study). CPOs in natural samples indicate two possible slip systems, [100](001) (Bezacier et al.,

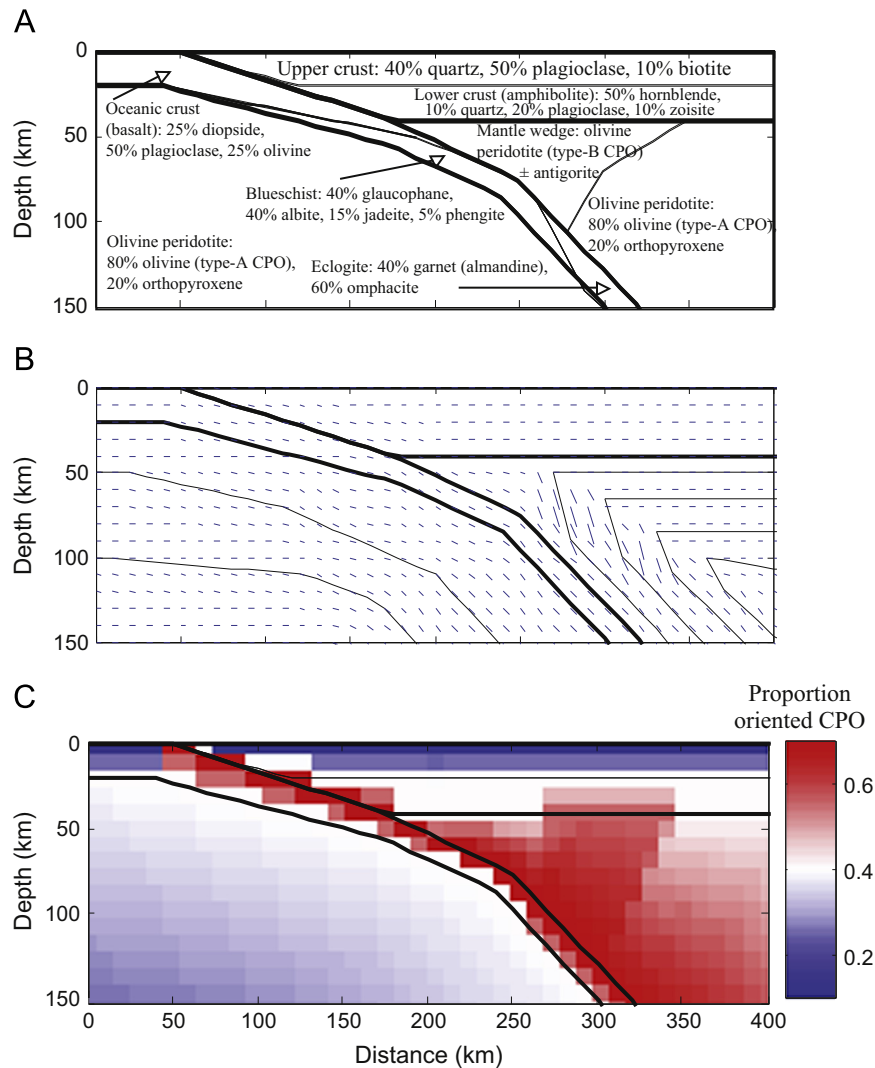


Fig. 7. Subduction-zone model. (A) Rock types, (B) orientation of foliation, lineation is within the plane of the section and (C) CPO strength.

2010; this study) and [010](001) (Hirauchi et al., 2010; Nishii et al., 2011; Jung, 2011; this study). The main difference in seismic properties between the two arises because the fast S-wave polarization direction is parallel to [100] for waves propagating perpendicular to the foliation. For CPOs with [100] parallel to the lineation, the fast shear-wave polarization plane for waves propagating perpendicular to the foliation is *parallel* to the lineation, and when [010] is parallel to the lineation the fast polarization plane is *perpendicular* to the lineation. Because of this difference, Jung (2011) suggested that dominance of the [010](001) slip system could help explain trench-parallel shear-wave splitting observations, even with a subhorizontal foliation. The elastic anisotropy of antigorite is controlled mainly by its layered structure, and V_{S1} and V_{S2} have similarly slow velocities for waves propagating perpendicular to $(001)_{atg}$ (i.e., perpendicular to the foliation for a deformation-induced CPO). The V_S anisotropy is only $\sim 1.6\%$ in this case, meaning that a horizontally foliated antigorite schist can only explain both the fast S-wave polarization direction *and* splitting times of > 1 s for SKS waves with near vertical propagation directions if there is > 200 km of 'single-crystal' antigorite.

A more likely scenario is that the mantle wedge contains a steep foliation composed of oriented olivine and antigorite. The high V_S anisotropy within, and V_{S1} polarization parallel to, the basal plane of the steeply dipping antigorite will contribute to both trench-parallel polarizations *and* large splitting times.

Hirauchi et al. (2010) suggested that a relatively thin (10–20 km) layer of steeply ($\sim 45^\circ$) dipping foliated antigorite could explain trench-parallel shear-wave splitting observations. This interpretation also relies on a rock composed of mainly antigorite. Perhaps most realistic would be a mantle wedge in which antigorite and olivine combine constructively to reinforce the magnitude of anisotropy and the fast S-wave polarization parallel to the trench.

4.6. Model subduction zone

To investigate the effects of topotaxy- vs. deformation-induced antigorite CPO in the mantle wedge of subduction zones we created a simplified model of a generic subduction zone, in which: (1) mineral assemblages are calculated using *Perple_X* (Connolly and Petrini, 2002; cf. Hacker, 2008), (2) foliation orientation is taken from the 2D corner flow models of Long et al. (2007) and Kneller et al. (2007), and (3) the CPOs are specified according to the predominant mineral slip systems, and the CPO strength varies with strain as calculated by Kneller et al. (2007) (Fig. 7).

The steps involved are:

- (1) *Specify the orientation of foliation and lineation at each grid point based on Long et al. (2007)*: The orientation of the foliation is specified to be subparallel to the maximum finite strain direction of Long et al. (2007). The lineation is in the

Table 2Mineral slip systems and C_{ij} used in model subduction zone. Full listing of elastic constants is found in Supplementary Table 1.

Mineral	Specified slip system	Elastic constants (C_{ij})
Quartz	Prism (a)	Quartz (Lakshtanov et al., 2007)
Plagioclase	[h0l](010)	An ₂₄ plagioclase (Ryzhova, 1964)
Albite	[h01](010)	An ₀₀ plagioclase (Ryzhova, 1964)
Biotite	[hk0](001)	Biotite (Aleksandrov and Ryzhova, 1961)
Phengite	[hk0](001)	Muscovite (Vaughan and Guggenheim, 1986)
Hornblende	[001](100)	Hornblende (Aleksandrov and Ryzhova, 1961)
Glaucophane	001	Glaucophane (Bezacier et al., 2010)
Omphacite	[001](010)	Di ₃₄ Jd ₆₆ clinopyroxene (Bhagat and Bass, 1992)
diopside	[001](010)	Di ₇₂ He ₀₉ d ₀₃ Cr ₀₃ Ts ₁₂ clinopyroxene (Collins and Brown, 1998)
Orthopyroxene	[001](010)	En ₇₅ Fs ₀₈ Ts ₁₂ orthopyroxene (Chai et al., 1997)
Jadeite	[001](010)	Jadeite (Kandelin and Weidner, 1988)
Olivine	A—[100](010); B—[001](010)	For ₉₀ olivine (Abramson et al., 1997)
Antigorite	[010](001)	Antigorite (Bezacier et al., 2010)
Zoisite	[010](001)	Zoisite (Mao et al., 2007)
Garnet	Random	Alm ₇₄ Py ₂₀ Gr ₃ Sp ₃ garnet (Babuska et al., 1978)

plane of the cross section because of the assumption of 2D flow.

- (2) *Create synthetic datasets of mineral preferred orientations expected from predominant mineral slip systems:* Synthetic CPO datasets are created such that the average crystallographic slip planes and slip directions (Table 2) are aligned with the specified foliation and lineation, respectively. For simplicity, only two olivine CPOs are considered, type-A and type-B, where type-B is in the areas of the mantle wedge specified by Kneller et al. (2007). The synthetic CPOs do not include asymmetry about the shear plane, which is common in olivine (e.g., Jung and Karato, 2001); including asymmetry results in rotations of $< 15^\circ$ about a horizontal axis and has minor effects on the calculated seismic properties of vertical column averages, which include a range of foliation dips.
- (3) *Vary CPO strength according to the finite-strain calculations of Long et al. (2007) and Kneller et al. (2007), such that high strain areas have the strongest CPOs:* CPO strength is varied by combining a synthetic strong CPO with a synthetic random CPO, such that there is a linear relationship between the magnitude of seismic anisotropy and the CPO strength (Supplementary Fig. 1), simplifying the process of relating observed seismic anisotropy to CPO strength.
- (4) *Combine synthetic EBSD datasets according to simplified mineral assemblages calculated using Perple_X, and calculate elastic properties for aggregate rock at each grid point using the Christoffel equation:* Aggregate elastic properties are calculated for each grid point individually using standard temperature and pressure elastic matrix constants, C_{ij} , listed in Table 2. Column averages are used to approximate vertically propagating rays; an over-simplification for SKS waves, but a reasonable first-order approximation. The effects of anisotropic layers are not considered in this approach, and are likely to be important.

To account for the effects of temperature and pressure, the calculated velocities are scaled according to the partial derivatives of the bulk and shear moduli of the aggregate with pressure and temperature using the Excel macro of Hacker and Abers, (2004), temperatures from Long et al. (2007), and pressure assuming a density of 3300 kg/m³. This isotropic scaling does not account for the effects of pressure and temperature on individual elastic constants, which are currently unconstrained in antigorite.

Results from 3 models are shown in Fig. 8. The first is a model subduction zone with no antigorite; the other two include 50 vol% antigorite in the mantle wedge in either topotactic orientation ((001)_{atg} || (100)_{ol}) or deformation-induced CPO ((001)_{atg} ||

foliation) (see Fig. 5). Fig. 8 shows V_p , V_p/V_{S1} , and shear-wave splitting times at each grid point for vertically propagating waves.

The model with no antigorite shows changes in V_p and V_s that are due to the changing foliation orientation rather than to changes in composition. The type-B olivine in this model leads to barely noticeable changes in V_p (Fig. 8A) but shows up as slightly lower V_p/V_s ratios (Fig. 8B). The distribution and magnitude of low V_p/V_s ratio is broadly consistent with seismic observations from beneath central Alaska (Rossi et al., 2006). Low V_p/V_s ratios are pronounced in areas of horizontal foliation for both type-A and type-B olivine CPO, which is consistent with observations of Hacker and Abers (2012). A zone of high V_p/V_s ratios is associated with nearly vertical foliation in which the olivine has type-A CPO. The highest shear-wave anisotropy in this model occurs within the “blueschist zone” of the subducting slab (Fig. 8C). The presence of type-B olivine CPO in the mantle wedge results in nearly trench-parallel fast S-wave polarization directions for the thickest, 50 km, part of the mantle wedge (Fig. 8D). The polarization directions are nearly parallel to the trench, and the calculated splitting time for the full 150 km column is ~ 1 s; the calculated splitting time is ~ 0.5 s for just the mantle wedge.

When 50 vol% antigorite is included, there are more noticeable effects. For topotactic antigorite, the mantle wedge has lower V_p , as expected (Fig. 8A). V_p/V_s ratios are significantly higher, particularly where the foliation is vertical (Fig. 8B). The shear-wave splitting times are high (0.05–0.04 s/km) throughout the mantle wedge when antigorite is topotactically related to type-B olivine CPO (Fig. 8C). Although the splitting times through the ~ 150 km column are high (~ 1 – 3 s) over the mantle wedge, the V_{S1} polarization directions are perpendicular to the trench (Fig. 8D).

For 50 vol% antigorite in a deformation-induced CPO, the reduction in V_p of vertically propagating waves is more apparent where the foliation is gently dipping (Fig. 8A). High V_p/V_s ratios are restricted to areas of the mantle wedge with a sub-horizontal foliation (Fig. 8B). This result is generally consistent with the results of Bostock et al. (2001) for an ‘inverted’ Moho separating faster lower crustal rocks from slower hydrated mantle in the Cascadia subduction zone. The model presented here does not have higher shear-wave velocities in the lower crust than the mantle, but shear-wave velocities are most dramatically decreased by horizontally foliated antigorite in the wedge tip, further illustrating the importance of considering anisotropy when interpreting seismic data. High V_s anisotropy is restricted to areas of the mantle wedge with a sub-vertical foliation (Fig. 8C), and in these areas the fast S-wave polarization plane is trench-parallel. The highest V_s anisotropy in this model is concentrated in an area that is ~ 20 km thick, and contains steeply dipping peridotite with

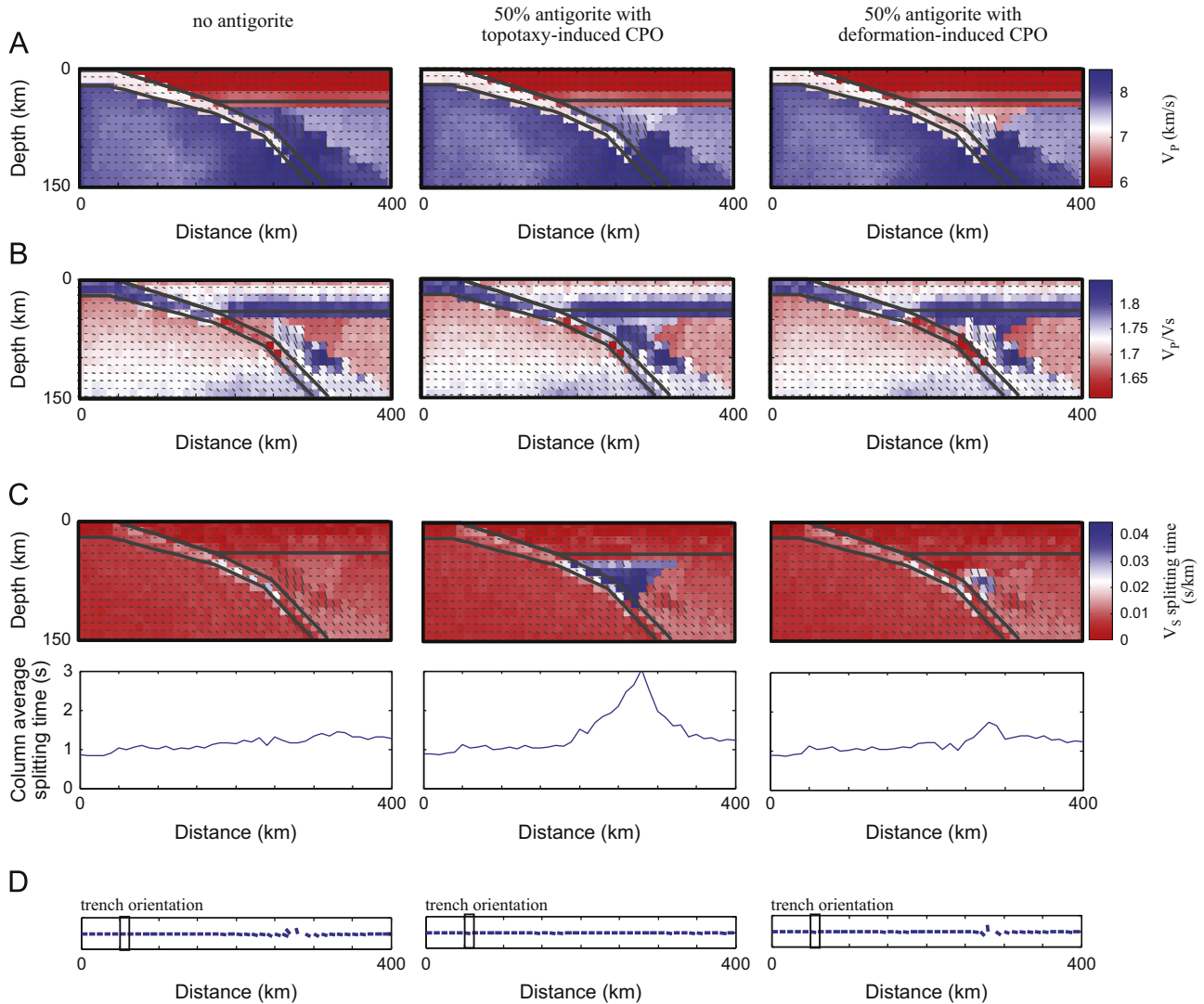


Fig. 8. Model results for no antigorite, 50 vol% antigorite in the mantle wedge in topotactic orientation, and 50% antigorite in deformation-induced CPO. (A) V_P calculated for vertically propagating waves. Antigorite in topotactic orientation is essentially invisible. (B) V_P/V_{S1} for waves propagating vertically through the wedge tip is lowest for unaltered peridotite, and highest for antigorite with deformation-induced CPOs. (C) V_S splitting times, $(1/V_{S2}-1/V_{S1})$, for vertically propagating waves are minimal for unaltered peridotite and antigorite with deformation-induced CPO, and maximized for antigorite topotactically replacing olivine. (D) Waves propagating vertically through forearc show 90° rotation of fast- V_S polarization planes for unaltered peridotite and antigorite with deformation-induced CPO, and no rotation for antigorite topotactically replacing olivine.

olivine type-B CPO and 50 vol% antigorite. The relatively small area of steeply dipping antigorite, combined with an olivine type-B CPO increases the shear-wave splitting time for the ~ 150 km column to ~ 1.5 – 2 s, and maintains fast S-wave polarization directions parallel to the trench (Fig. 8D). *These results indicate that a combination of olivine type-B CPO, and antigorite oriented with (001) parallel to the foliation can produce significant V_S anisotropy and trench-parallel fast S-wave polarization directions in a mantle wedge with a thin layer (~ 20 km thick) in which the foliation is steep.*

The above models assume that the olivine in the mantle wedge has a type-B CPO. If trench-parallel flow with olivine type-E CPO (e.g., Mehl et al., 2003) is assumed, the model results do not change significantly. Topotactic growth of antigorite into sub-horizontally foliated type-E olivine results in an initial decrease in V_S anisotropy followed by a rotation of the fast S-wave polarization direction from trench-parallel to trench-perpendicular with increasing vol% antigorite. Therefore, trench-parallel shear-wave splitting directions with large ($\sim > 1$ s) splitting times are more consistent with antigorite in a zone with

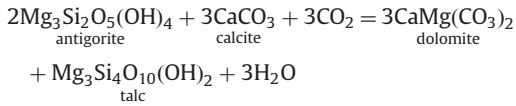
steeply dipping foliation. Because such a small zone of antigorite in the mantle wedge may represent a significant contribution to shear-wave splitting, the methods used to image that particular feature must be adjusted. Shear-wave splitting of long-wavelength SKS waves is not ideally suited for imaging small features. Shear-wave splitting from local earthquakes, such as those occurring in the slab (e.g. Wirth and Long, 2010), could provide high frequency seismic energy that would be sensitive to smaller-scale features in the mantle wedge.

Antigorite CPOs from rocks show the effects of both topotactic growth (e.g. (001) girdles) and deformation, with [001] maxima orthogonal to the foliation. Because the initial effects of topotaxy are to decrease the velocity anisotropy of a peridotite (Fig. 6B), the presence of topotactic antigorite will contribute to spatial variability in V_S anisotropy (e.g., Huang et al., 2011) in areas of olivine hydration. The relative importance of topotaxy vs. deformation in controlling antigorite CPO is likely to be related to a number of factors, including the degree of alteration (i.e., vol% antigorite), temperature, pressure, and strain. More experiments, in particular deformation experiments on olivine containing topotactic

antigorite, are needed to understand how antigorite forms and deforms in mantle wedges. If antigorite instead forms dominantly as veins with girdle distributions of (001)_{atg}, its effects on seismic anisotropy may be less pronounced.

4.7. Carbonation

The vein of dolomite and antigorite in MVE03–60 is suggestive of a carbonation/dehydration reaction such as



It is difficult to tell from the small area of this EBSD map (Fig. 4) whether dolomite grew into voids around antigorite or whether antigorite grew into and replaced dolomite. All of these minerals are present in the sample (CaCO₃ is present in the sample, but not present in this fine scale map) and the strong CPOs of dolomite and antigorite produce a distinct seismic signature (Fig. 4G; dolomite C_{ij} from Humbert and Plicque (1972)). Such a rock has high V_p anisotropy (27%), similar in magnitude to sheared antigorite, but the maximum V_s anisotropy is ~33% lower than for pure sheared antigorite. The V_p/V_s ratio is 1.56–1.94 compared to 1.46–1.81 for pure antigorite with the observed CPO (MVE03–20–4). This suggests that decarbonation and dehydration of hydrated oceanic crust and carbonate sediments within the subducting slab can contribute to seismic anisotropy in a carbonated and hydrated mantle wedge.

5. Conclusions

Antigorite serpentinites from the Motagua fault zone in central Guatemala display CPOs of varying strengths (Fig. 3). The variation in CPO strength is due to variations in strain, which orients (001)_{atg} parallel to the shear plane. Two samples show diffuse (001)_{atg} girdles, which may be related to the growth of antigorite in a vein, or to topotactic growth on olivine, suggesting that antigorite may retain information about the CPO of the host from which it grew. Topotactic relationships observed by Boudier et al. (2010) suggest that [010]_{atg} grows parallel to [001]_{ol}, whereas two possible orientations of (001)_{atg} can occur, the dominant orientation being (001)_{atg}||[100]_{ol}. Because [010]_{atg} has only one topotactic orientation with respect to olivine, antigorite grown topotactically in olivine should have a stronger [010]_{atg} preferred orientation than (001)_{atg}; this is observed in many of the samples in this study. In the two samples where the foliation was clearly identifiable, there are two different orientations of [010]_{atg} with respect to the lineation. In MVE03–20–4 [010]_{atg} is parallel to the lineation, and in MVJ84–3–1 [100]_{atg} is parallel to the lineation. Both of these orientations have been observed separately (e.g., Bezacier et al., 2010; Hirauchi et al., 2010), but this is the first study to report both CPOs in natural antigorite samples.

The velocities calculated from these CPOs have varying degrees of anisotropy. For all samples the slowest waves are those propagating perpendicular to (001)_{atg}. The samples with the strongest preferred orientation of (001)_{atg} have the highest anisotropy in both V_p and V_s —28% in V_p and 33% in V_s . For samples with V_s anisotropy greater than ~6%, the velocity symmetry is approximately uniaxial, with a unique slow axis perpendicular to the foliation. These results suggest that where foliated antigorite is present, high shear-wave anisotropy will be observed for waves propagating parallel to the foliation. In contrast, topotactic growth of antigorite in olivine produces a high shear-wave anisotropy perpendicular to the shear direction, and vein growth of antigorite

is likely to produce minimal anisotropy. Given our observations, the best explanation for significant V_s anisotropy and trench-parallel fast S-wave polarization directions in a mantle wedge is a thin (~20 km thick) layer with a steep foliation and an olivine type-B CPO plus antigorite with (001) parallel to the foliation produced by deformation.

EBSD measurements from a dolomite+antigorite vein suggest that carbonation of hydrated peridotite may produce high seismic anisotropy. More observations are needed, in particular in rocks with measurable foliation and lineation.

Acknowledgments

GEH is pleased to acknowledge funding from NSF through awards EAR0309320 and EAR1119403 in support of this research. BRH and SJB were supported by NSF Grants EAR-0607775 and EAR-0745588, and the University of California, Santa Barbara. We acknowledge the work of 3 anonymous reviewers that helped to improve this manuscript.

Appendix A. Supplementary information

Supplementary data associated with this article can be found in the online version at <http://dx.doi.org/10.1016/j.epsl.2013.06.003>.

References

- Abramson, E.H., Brown, J.M., Slutzky, L.J., Zaugg, J., 1997. The elastic constants of San Carlos olivine to 17 GPa. *J. Geophys. Res.* 102, 12253–12263.
- Aleksandrov, K.S., Ryzhova, T.V., 1961. The elastic properties of rock-forming minerals: II layered silicates. *Izv. Acad. Sci. USSR, Phys. Solid Earth* 12, 1165–1168. (English translation).
- Aruja, E., 1945. An X-ray study of the crystal-structure of antigorite. *Mineral. Mag.* 27, 65–74.
- Auzende, A.-L., Pellenq, R.J.-M., Devouard, B., Baronnet, A., Grauby, O., 2006. Atomistic calculations of structural and elastic properties of serpentine minerals: the case of lizardite. *Phys. Chem. Miner.* 33, 266–275.
- Babuska, V., Fiala, J., Kumazawa, M., Ohno, I., Sumino, Y., 1978. Elastic properties of garnet solid-solution series. *Phys. Earth Planet. Inter.* 16, 157–176.
- Baccheschi, P., Margheriti, L., Steckler, M.S., Boschi, E., 2011. Anisotropy patterns in the subducting lithosphere and in the mantle wedge: a case study—the southern Italy subduction system. *J. Geophys. Res.* 116, B08306, <http://dx.doi.org/10.1029/2010JB7961>.
- Ben Ismail, W., Mainprice, D., 1998. An olivine fabric database: and overview of upper mantle fabrics and seismic anisotropy. *Tectonophysics* 296, 145–157.
- Bezacier, L., Reynard, B., Bass, J.D., Sanchez-Valle, C., Van de Moortele, B., 2010. Elasticity of antigorite, seismic detection of serpentinites, and anisotropy in subduction zones. *Earth Planet. Sci. Lett.* 289, 198–208.
- Bhagat, S.S., Bass, J.D., 1992. Single-crystal elastic properties of omphacite-C2/c by Brillouin spectroscopy. *J. Geophys. Res.* 97, 6843–6848.
- Bostock, M.G., Hyndman, R.D., Rondenay, S., Peacock, S.M., 2001. An inverted continental Moho and serpentinization of the forearc mantle. *Nature* 417, 536–538.
- Boudier, F., Baronnet, A., Mainprice, D., 2010. Serpentine mineral replacements of natural olivine and their seismic implications: oceanic lizardite versus subduction-related antigorite. *J. Petrol.* 51, 495–512.
- Bruceckner, H.K., Avé Lallemant, H.G., Sisson, V.B., Harlow, G.E., Hemming, S.R., Sorensen, S.S., Tsujimori, T., Martens, U., 2009. Metamorphic reworking of a high-pressure–low temperature mélange along the Motagua fault, Guatemala: a revised record of Neocomian and Maastrichtian transpressional tectonics. *Earth Planet. Sci. Lett.* 284, 228–235.
- Brudzinski, M.R., Thurber, C.H., Hacker, B.R., Engdahl, E.R., 2007. Global prevalence of double Benioff zones. *Science* 316, 1472–1474.
- Capitani, G.C., Mellini, M., 2004. The modulated crystal structure of antigorite: the $m=17$ polysome. *Am. Mineral.* 89, 147–158.
- Chai, M., Brown, J., Slutzky, L.J., 1997. The elastic constants of an aluminous orthopyroxene to 12.5 GPa. *J. Geophys. Res.* 102, 14779–14785.
- Collins, M.D., Brown, J.M., 1998. Elasticity of an upper mantle pyroxene. *Phys. Chem. Miner.* 26, 7–13.
- Connolly, J.A.D., Pettrini, K., 2002. An automated strategy for calculation of phase diagram sections and retrieval of rock properties as a function of physical conditions. *J. Metamorph. Geol.* 20, 697–708, <http://dx.doi.org/10.1046/j.1525-1314.2002.00398.x>.

- Conrad, C.P., Behn, M.D., Silver, P.G., 2007. Global mantle flow and the development of seismic anisotropy: differences between the oceanic and continental upper mantle. *J. Geophys. Res.* 112, B07317, <http://dx.doi.org/10.1029/2006JB004608>.
- Day, A.P., 2008. Spherical EBSD. *J. Microsc.* 230, 472–486.
- Delle Piane, C., Burlini, L., Kunze, K., 2009. The influence of dolomite on the plastic flow of calcite: rheological, microstructural and chemical evolution during large strain torsion experiments. *Tectonophysics* 467, 145–166.
- Evans, B.E., 1977. Metamorphism of alpine peridotite and serpentinite. *Annu. Rev. Earth Planet. Sci.* 5, 397–447.
- Flores, K.E., Harlow, G.E., Sisson, V.B., Stampfli, G.M., 2010. Tectonic origin and evolution of the Central American high-pressure/low-temperature serpentinite mélanges: a new 3D Geodynamic Scenario. Abstracts with Programs, Annual Meeting, Geological Society of America, vol. 42, No. 5, 679. (<http://a-c-s.confex.com/crops/2010am/webprogram/Paper179220>).
- Fontaine, F.R., Hoof, E.E.E., Burkett, P.G., Toomey, D.R., Solomon, S.C., Silver, P.G., 2005. Shear-wave splitting beneath the Galapagos archipelago. *Geophys. Res. Lett.* 32, L21308, <http://dx.doi.org/10.1029/2005GL024014>.
- Frese, K., Trommsdorff, V., Kunze, K., 2003. Olivine [100] normal to foliation: lattice preferred orientation in prograde garnet peridotite formed at high H₂O activity, Cima di Gagnone (Central Alps). *Contrib. Mineral. Petrol.* 145, 75–86.
- Funicello, F., Moroni, M., Piromallo, C., Faccenna, C., Cenedese, A., Bui, H.A., 2006. Mapping mantle flow during retreating subduction: laboratory models analyzed by feature tracking. *J. Geophys. Res.* 111, B03402, <http://dx.doi.org/10.1029/2005JB003792>.
- Groppo, C., Compagnoni, R., 2007. Ubiquitous fibrous antigorite veins from the Lanzo Ultramafic Massif, Internal Western Alps (Italy): characterization and genetic conditions. *Per. Mineral.* 76, 169–181.
- Hacker, B.R., 2008. H₂O subduction beyond arcs. *Geochem. Geophys. Geosyst.* 9, Q03001, <http://dx.doi.org/10.1029/2007GC001707>.
- Hacker, B.R., Abers, G.A., 2004. Subduction Factory 3: an Excel worksheet and macro for calculating the densities, seismic wave speeds, and H₂O contents of minerals and rocks at pressure and temperature. *Geochem. Geophys. Geosyst.* 5, Q01005, <http://dx.doi.org/10.1029/2003GC000614>.
- Hacker, B.R., Abers, G.A., 2012. Subduction Factory 5: unusually low Poisson's ratios in subduction zones from elastic anisotropy of peridotite. *J. Geophys. Res.* 117, B06308, <http://dx.doi.org/10.1029/2012JB009187>.
- Hacker, B.R., Peacock, S.M., Abers, G.A., Holloway, S.D., 2003. Are intermediate-depth earthquakes in subducting slabs linked to metamorphic dehydration reactions? *J. Geophys. Res.* 108, B1, <http://dx.doi.org/10.1029/2001JB001129>.
- Harlow, G.E., Brueckner, H.K., Sorensen, S.S., 2009. Serpentinities of the Motagua fault zone mélanges, Guatemala: an assessment. Abstracts with Programs, Annual Meeting, Geological Society of America, vol. 42, No. 5, 2010, 679. (<http://a-c-s.confex.com/crops/2010am/webprogram/Paper181532>).
- Harlow, G.E., Price, N.A., Tsujimori, T., 2006. Serpentinities of the Motagua fault zone, Guatemala: a mineralogical assessment. Program with Abstracts, 19th General Meeting of the International Mineralogical Association, 23–28 July 2006, Kobe, Japan, P19-17, 223.
- Harlow, G.E., Sisson, V.B., Sorensen, S.S., 2011. Jadeite from Guatemala: distinctions among multiple occurrences. *Geol. Acta* 9 (3), 363–387.
- Higgs, D.V., Handin, J., 1959. Experimental deformation of dolomite single crystals. *Geol. Soc. Am. Bull.* 70, 245–278.
- Hirauchi, K., Michibayashi, K., Ueda, H., Katayama, I., 2010. Spatial variations in antigorite fabric across a serpentine subduction channel: insights from the Ohmachi Seamount, Izu–Bonin frontal arc. *Earth Planet. Sci. Lett.* 299, 196–206.
- Huang, Z., Zhao, D., Wang, L., 2011. Seismic heterogeneity and anisotropy of the Honshu arc from the Japan Trench to the Japan Sea. *Geophys. J. Int.* 184, 1428–1444.
- Humbert, P., Plicque, F., 1972. Elastic properties of monocrystalline rhombohedral carbonates – calcite, magnesite, dolomite. *C. R. Acad. Sci. Ser. B* 275, 391.
- Jung, H., 2011. Seismic anisotropy produced by serpentine in mantle wedge. *Earth Planet. Sci. Lett.* 307, 535–543.
- Jung, H., Karato, S., 2001. Water-induced fabric transitions in olivine. *Science* 293, 1460–1463.
- Jung, H., Katayama, I., Jiang, Z., Hiraga, T., Karato, S., 2006. Effect of water and stress on the lattice-preferred orientation of olivine. *Tectonophysics* 421, 1–22.
- Kandelin, J., Weidner, D.J., 1988. The single crystal elastic properties of jadeite. *Phys. Earth Planet. Inter.* 50, 251–260.
- Karato, S., Jung, H., Katayama, I., Skemer, P., 2008. Geodynamic significance of seismic anisotropy of the upper mantle: new insights from laboratory studies. *Annu. Rev. Earth Planet. Sci.* 36, 59–95.
- Katayama, I., Hirauchi, K., Michibayashi, K., Ando, J., 2009. Trench-parallel anisotropy produced by serpentine deformation in the hydrated mantle wedge. *Nature* 461, 1114–1118.
- Katayama, I., Karato, S., 2008. Low-temperature, high-stress deformation of olivine under water-saturated conditions. *Phys. Earth Planet. Inter.* 168, 125–133.
- Katayama, I., Karato, S., Brandon, M., 2005. Evidence of high water content in the deep upper mantle inferred from deformation microstructures. *Geology* 33, 613–616.
- Kneller, E.A., Long, M.D., van Keken, P.E., 2008. Olivine fabric transitions and shear wave anisotropy in the Ryukyu subduction system. *Earth Planet. Sci. Lett.* 268, 268–282.
- Kneller, E.A., van Keken, P.E., Katayama, I., Karato, S., 2007. Stress, strain, and B-type olivine fabric in the fore-arc mantle: sensitivity tests using high-resolution steady-state subduction zone models. *J. Geophys. Res.* 112, B04406, <http://dx.doi.org/10.1029/2006JB004544>.
- Krieger Lassen, N.C., 1998. Automatic high-precision measurements of the location and width of Kikuchi bands in electron backscatter diffraction patterns. *J. Microsc.* 190, 375–391.
- Lakshtanov, D.L., Seinogeikin, S.V., Bass, J.D., 2007. High-temperature phase transitions and elasticity of silica polymorphs. *Phys. Chem. Miner.* 34, 11–22.
- Livi, K.J.T., Veblen, D.R., 1987. "Eastonite" from Easton, Pennsylvania: a mixture of phlogopite and a new form of serpentine. *Am. Mineral.* 72, 113–125.
- Long, M.D., 2010. Frequency-dependent shear wave splitting and heterogeneous anisotropic structure beneath the Gulf of California region. *Phys. Earth Planet. Inter.* 182, 59–72.
- Long, M.D., Hager, B.H., de Hoop, M.V., van der Hilst, R.D., 2007. Two-dimensional modeling of subduction zone anisotropy with application to southwestern Japan. *Geophys. J. Int.* 170, 839–856.
- Long, M.D., van der Hilst, R.D., 2006. Shear wave splitting from local events beneath the Ryukyu arc: trench-parallel anisotropy in the mantle wedge. *Phys. Earth Planet. Inter.* 155, 300–312.
- Mainprice, D., 1990. A FORTRAN program to calculate seismic anisotropy from the lattice preferred orientation of minerals. *Comput. Geosci.* 16, 385–393.
- Mao, Z., Jiang, F.M., Duffy, T.S., 2007. Single crystal elasticity of zoisite Ca₂Al₃Si₃O₁₂(OH) by Brillouin scattering. *Am. Mineral.* 92, 570–576.
- Mehl, L., Hacker, B.R., Hirth, G., Kelemen, P.B., 2003. Arc-parallel flow within the mantle wedge: evidence from the accreted Talkeetna arc, south central Alaska. *J. Geophys. Res.* 108, 2375–2393, <http://dx.doi.org/10.1029/2002JB002233>.
- Mizukami, T., Wallis, S.R., Yamamoto, J., 2004. Natural examples of olivine lattice preferred orientation patterns with a flow-normal α -axis maximum. *Nature* 427, 432–436.
- Nakajima, J., Hasegawa, A., 2004. Shear-wave polarization anisotropy and subduction-induced flow in the mantle wedge of northeastern Japan. *Earth Planet. Sci. Lett.* 225, 365–377.
- Nishii, A., Wallis, S.R., Mizukami, T., Michibayashi, K., 2011. Subduction related antigorite CPO patterns from forearc mantle in the Sanbagawa belt, southwest Japan. *J. Struct. Geol.* 33, 1436–1445.
- Padrón Navarta, J.A., Tommasi, A., Garrido, C.J., Sanchez-Vizcaíno, V.L., 2012. Plastic deformation and development of antigorite crystal preferred orientation in high pressure serpentinites. *Earth Planet. Sci. Lett.* 349–350, 75–86.
- Park, J., Levin, V., 2002. Seismic anisotropy: tracing plate dynamics in the mantle. *Science* 296, 485–489.
- Rabbal, W., Koulakov, I., Dinc, A.N., Jakovlev, A., 2011. Arc-parallel shear deformation and escape flow in the mantle wedge of the Central America subduction zone: evidence from P wave anisotropy. *Geochem. Geophys. Geosyst.* 12, Q05S31, <http://dx.doi.org/10.1029/2010GC003325>.
- Rossi, G., Abers, G.A., Rondenay, S., Christensen, D.H., 2006. Unusual mantle Poisson's ratio, subduction, and crustal structure in central Alaska. *J. Geophys. Res.* 111, B09311, <http://dx.doi.org/10.1029/2005JB003956>.
- Ryzhova, T.V., 1964. Elastic properties of plagioclase. *Izv. Geophys. Ser.* 7, 1049–1051.
- Savage, M.K., 1999. Seismic anisotropy and mantle deformation: what have we learned from shear wave splitting? *Rev. Geophys.* 37, 65–106.
- Skemer, P., Katayama, I., Karato, S., 2006. Deformation fabrics of the Cima di Gagnone peridotite massif, Central Alps, Switzerland: evidence of deformation at low temperatures in the presence of water. *Contrib. Mineral. Petrol.* 152, 43–51.
- Smith, G.P., Wiens, D.A., Fischer, K.M., Dorman, L.M., Webb, S.C., Hildebrand, J.A., 2001. A complex pattern of mantle flow in the Lau backarc. *Science* 292, 713–716.
- Soda, Y., Takagi, H., 2010. Sequential deformation from serpentinite mylonite to metasomatic rocks along the Sashu Fault, SW Japan. *J. Struct. Geol.* 32, 792–802.
- Van de Moortele, B., Bezacier, L., Trullenque, G., Reynard, B., 2010. Electron back-scattering diffraction (EBSD) measurements of antigorite lattice-preferred orientations (LPO). *J. Microsc.* 239, 245–248.
- Vaughan, M.T., Guggenheim, S., 1986. Elasticity of muscovite and its relation to crystal structure. *J. Geophys. Res.* 91, 4657–4664.
- Wirth, E., Long, M.D., 2010. Frequency-dependent shear wave splitting beneath the Japan and Izu–Bonin subduction zones. *Phys. Earth Planet. Inter.* 181, 141–154.
- Wolfe, C.J., Silver, P.G., 1998. Seismic anisotropy of oceanic upper mantle: shear wave splitting methodologies and observations. *J. Geophys. Res.* 103, 749–771.